



Cite this: *Catal. Sci. Technol.*, 2019, 9, 6884

## Chemoselective reduction of quinoline over Rh-C<sub>60</sub> nanocatalysts†

Zhishan Luo,<sup>a</sup> Yuanyuan Min,<sup>a</sup> Divya Nechiyl,<sup>b</sup> Wolfgang Bacsá,<sup>b</sup> Yann Tison,<sup>c</sup> Hervé Martinez, <sup>c</sup> Pierre Lecante, <sup>b</sup> Iann C. Gerber, <sup>d</sup> Philippe Serp<sup>a</sup> and M. Rosa Axet \*<sup>a</sup>

The design and engineering of heterogeneous nanocatalysts that are both highly active and selective for hydrogenation reactions constitute a crucial challenge. In that context, herein a series of Rh-C<sub>60</sub> nanocatalysts have been synthesized *via* the decomposition of an organometallic rhodium complex in the presence of fullerene C<sub>60</sub> under a H<sub>2</sub> atmosphere. Rhodium atomically dispersed or rhodium nanoparticles on Rh-C<sub>60</sub> spherical fulleride particles were produced by tuning the Rh/C<sub>60</sub> molar ratio. Significant charge transfer between rhodium and C<sub>60</sub> was evidenced through Raman and X-ray photoelectron spectroscopy, which indicates electron-deficient Rh species. The resulting heterostructured nanomaterials were applied successfully in the catalytic hydrogenation of quinoline, exhibiting excellent activity and producing selectively the partially hydrogenated product, 1,2,3,4-tetrahydroquinoline. Density functional theory (DFT) calculations show that the hydride coverage of the Rh NPs plays a key role in the adsorption modes of quinoline and 1,2,3,4-tetrahydroquinoline on the surface of the NPs, and that these adsorption modes are modulated by the presence of fullerene C<sub>60</sub>, thus affecting the activity and selectivity obtained with this rhodium based catalyst.

Received 8th October 2019,  
Accepted 30th October 2019

DOI: 10.1039/c9cy02025j

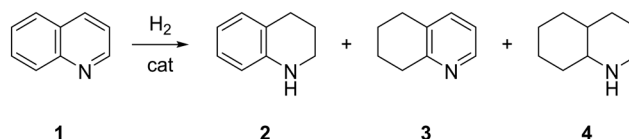
rsc.li/catalysis

## Introduction

Heterogeneous catalytic hydrogenation reactions are broadly known as one of the most fundamental chemical transformations in both the laboratory and industry.<sup>1–5</sup> Over the years, numerous heterogeneous nanocatalysts, in particular, carbon-based hybrid nanostructures, have shown high catalytic activity and selectivity in hydrogenation reactions,<sup>6–12</sup> owing to their high surface area to volume ratio, exclusive electronic properties to favour charge transfer, high chemical and thermal stability, ease of recovery from the reaction mixture and high mechanical strength. Catalytic reduction of quinoline (1) is a key organic reaction where one of the products, 1,2,3,4-tetrahydroquinoline (2), is an important intermediate for pharmaceuticals, agrochemicals, alkaloids and various biological active molecules.<sup>13–16</sup> In

particular, quinolines allow the preparation of tetrahydroquinoline products that are broadly found in drug molecules.<sup>14,16</sup> A simple and effective synthesis strategy is the direct regioselective hydrogenation of quinoline (Scheme 1). However, 5,6,7,8-tetrahydroquinoline (3) and the fully hydrogenated product decahydroquinoline (4) may be also produced.

A variety of heterogeneous catalysts have been developed to improve activity and selectivity for this reaction in recent years. Au,<sup>17</sup> Rh,<sup>18–25</sup> Ru,<sup>26,27</sup> Pd (ref. 28) and Pt (ref. 29)-based catalysts have been revealed to be very active and selective. Specifically, Rh nanoparticles (NPs) show high selectivity towards 1,2,3,4-tetrahydroquinoline (2). For instance, rhodium NPs immobilized in a Lewis acidic ionic liquid (IL) catalyse a large scope of heteroarenes, being very selective to the arene ring without hydrogenating other functional groups.<sup>23</sup> In the specific case of quinoline, it was selectively hydrogenated to 2 (95% yield) at 30 bar of H<sub>2</sub> and 80 °C after 15 h of reaction. Other Rh catalysts have produced the partial



Scheme 1 Hydrogenation of quinoline.

<sup>a</sup> LCC-CNRS, Université de Toulouse, CNRS, INPT, Toulouse, France.

E-mail: rosa.axet@lcc-toulouse.fr

<sup>b</sup> Centre d'Élaboration des Matériaux et d'Études Structurales UPR CNRS 8011, 29 Rue Jeanne-Marvig, BP 4347, 31055 Toulouse, France

<sup>c</sup> CNRS/UNIV PAU & PAYS ADOUR/E2S UPPA, Institut des Sciences Analytiques et de Physicochimie pour l'Environnement et les Matériaux, UMR5254, 64000, Pau, France

<sup>d</sup> LPCNO, Université de Toulouse, INSA-CNRS-UPS, 135 Avenue de Rangueil, 31077 Toulouse, France

† Electronic supplementary information (ESI) available. See DOI: 10.1039/c9cy02025j

hydrogenated product **2** very selectively under similar reaction conditions: Rh NPs over reduced graphene oxide (99% yield; 30 bar of H<sub>2</sub>, 80 °C, 12 h);<sup>25</sup> Rh NPs stabilized with polyethylene glycol (99% selectivity; 30 bar of H<sub>2</sub>, 100 °C, 3 h);<sup>22</sup> Rh NPs stabilized with a phosphine-functionalized IL (99% selectivity; 30 bar of H<sub>2</sub>, 50 °C, 5 h);<sup>21</sup> Rh NPs stabilized with tannin (94% selectivity; 20 bar of H<sub>2</sub>, 80 °C, 0.5 h).<sup>19</sup> Interestingly, the Rh/AlO(OH)<sup>18</sup> catalyst and Rh NPs stabilized with an N-heterocyclic carbene (NHC)<sup>24</sup> were able to hydrogenate quinoline under milder reaction conditions. Rh/AlO(OH) was active at room temperature using a hydrogen balloon and produced **2** with a selectivity of 94% after 6 h of reaction. Rh-NHC was also active at low temperature (30 °C) under 20 bar of H<sub>2</sub> pressure reaching full conversion after 140 min of reaction, but in this case, only 75% selectivity to **2** was observed (TOF = 238 h<sup>-1</sup>). Full conversion after only 30 min of reaction was achieved by increasing the temperature to 60 °C and quinoline was completely consumed with 75% selectivity towards **2**; after 24 hours of reaction, the fully reduced product **4** was obtained (TOF = 496 h<sup>-1</sup>). These last two examples describe very active catalysts able to produce the fully hydrogenated decahydroquinoline (Rh/AlO(OH)) under slightly harsher reaction conditions (8 bar of H<sub>2</sub>, 100 °C, 5 h),<sup>20</sup> which is in opposition to the findings using Rh NPs immobilized in a Lewis acidic IL.<sup>23</sup> These results suggest that electron-rich Rh NPs are very active, but, in general, less selective to the partially hydrogenated product **2**.

On the other hand, electron-poor Ru NPs can be produced straightforwardly from the decomposition of (1,5-cyclooctadiene)(1,3,5-cyclooctatriene)ruthenium(0) [Ru(COD)(COT)] with H<sub>2</sub> in the presence of fullerene C<sub>60</sub>.<sup>30</sup> This nanocatalyst shows excellent activity and selectivity in the hydrogenation of nitrobenzene.<sup>31,32</sup> The same methodology has been used to obtain other metal NPs.<sup>33</sup> Also, fullerene C<sub>60</sub> based catalysts with other metals have been described,<sup>34</sup> including Pd,<sup>35</sup> Ni (ref. 36) and Ru.<sup>37,38</sup> With the ability of fullerene to accommodate various metals,<sup>39</sup> as well as the effectiveness of the organometallic approach to produce almost any kind of noble metal NP, we decided to synthesize Rh-C<sub>60</sub> catalysts with the aim of producing electron-poor Rh NPs, which can be very interesting for selective quinoline hydrogenation.<sup>23,25</sup> In this work, we demonstrate that rhodium NPs can be synthesized straightforwardly *via* the decomposition of the [Rh(η<sup>3</sup>-C<sub>3</sub>H<sub>5</sub>)<sub>3</sub>] complex in the presence of fullerene C<sub>60</sub> in 1,2-dichlorobenzene (DCB) under a H<sub>2</sub> atmosphere. Rh atomically dispersed or Rh NPs on Rh-C<sub>60</sub> fulleride spherical particles were produced by tuning the ratio of the Rh precursor and fullerene. These Rh compounds were characterized using several techniques such as transmission electron microscopy (TEM), wide angle X-ray scattering (WAXS), inductively coupled plasma optical emission spectroscopy (ICP-OES), attenuated total reflection infrared spectroscopy (ATR-IR), solid-state NMR (SSNMR), and thermal gravimetric analysis (TGA), including X-ray photoelectron spectroscopy (XPS) and Raman spectroscopy,

which evidenced charge transfer from rhodium to fullerene. The nanostructures were used as catalysts in the hydrogenation of quinoline, showing excellent activity (TOF = 488.0 h<sup>-1</sup>) and selectivity to **2** (up to 98%). Density functional theory (DFT) calculations were also performed to support these findings.

## Results and discussion

A series of Rh-C<sub>60</sub> compounds were synthesised through the decomposition of [Rh(η<sup>3</sup>-C<sub>3</sub>H<sub>5</sub>)<sub>3</sub>] under 3 bars of H<sub>2</sub> in the presence of C<sub>60</sub> using 1,2-dichlorobenzene (DCB) as a solvent at 50 °C. In this series, the molar Rh/C<sub>60</sub> ratio has been varied ranging from [Rh]/[C<sub>60</sub>] = 1 to 20. Fig. 1 shows the representative TEM images of the as-synthesised products. Nanospheres with a size of about 100–170 nm were observed, which were decorated with Rh NPs (Fig. 1 and S1† and Table 1). The NP size was in the range of 2–3 nm, presenting a broad size distribution (polydispersities of around 30%), which displays a bimodal distribution for samples 5/1 and 10/1. These species are structurally similar to the ruthenium nanocatalysts stabilized with fullerene C<sub>60</sub> described in a previous study by some of us.<sup>30</sup> In the above-mentioned work, the decomposition of [Ru(COD)(COT)] under dihydrogen in the presence of fullerene C<sub>60</sub> provided a Ru based catalyst composed of Ru-C<sub>60</sub> molecular spheres with their surface decorated with Ru NPs, as pointed out by a combination of characterization techniques, including TEM, WAXS, and extended X-ray absorption fine structure (EXAFS), and supported by DFT calculations. Also, Ru-C<sub>60</sub> fulleride nanospheres synthesised in DCB displayed a size of 200.0 ± 38.5 nm, which is similar to the ones of Rh-C<sub>60</sub> materials. Furthermore, HRTEM analyses were performed for the Rh-C<sub>60</sub> 1/1 and 10/1 samples. The HAADF-STEM mode allowed the detection of a few Rh NPs on the surface of the nanospheres in the Rh-C<sub>60</sub> 1/1 compound, together with isolated atoms on the surface, which was in contrast with the

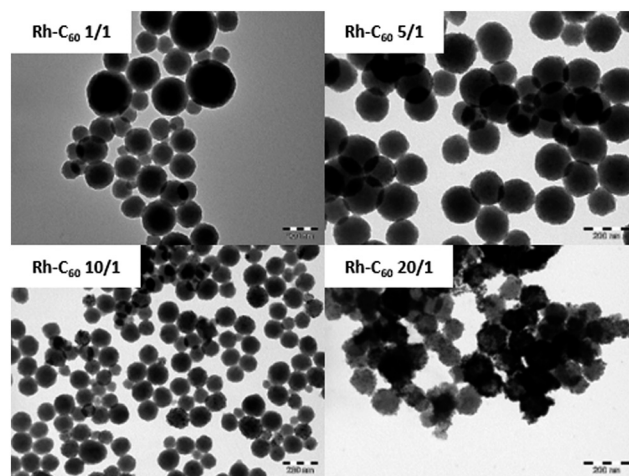
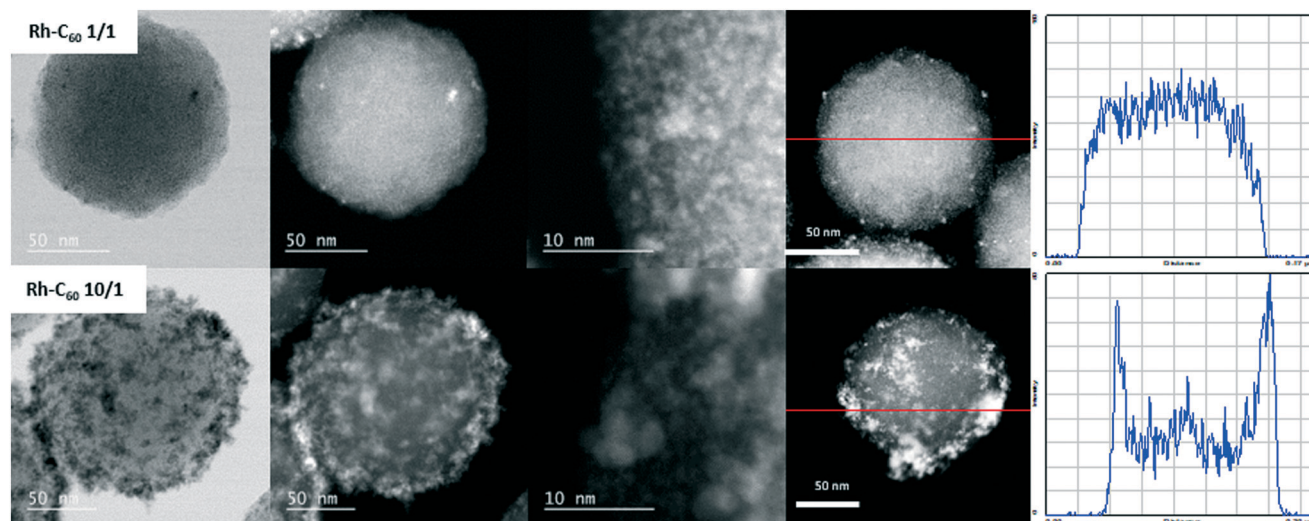


Fig. 1 TEM micrographs of Rh-C<sub>60</sub> 1/1, 5/1, 10/1, and 20/1 (scale bar 200 nm).

**Table 1** Mean size distributions and rhodium content of the Rh-C<sub>60</sub> nanocatalyst

Rh-C <sub>60</sub>	Rh content <sup>a</sup> (%)	NP mean size <sup>b</sup> (nm)	Nanosphere mean size <sup>b</sup> (nm)
1/1	9.2	2.0 ± 0.4	158.2 ± 27.5
5/1	23.3	1.1 ± 0.3 (21%)/3.0 ± 0.9 (79%) <sup>c</sup>	103.0 ± 15.5
10/1	35.9	1.9 ± 0.5 (69%)/4.7 ± 1.1 (31%) <sup>c</sup>	167.9 ± 27.3
20/1	46.2	2.3 ± 0.6	96.3 ± 14.4

<sup>a</sup> By ICP. <sup>b</sup> Manual measurements from enlarged TEM micrographs of at least 150 objects. <sup>c</sup> In brackets is the percentage of each population.



**Fig. 2** STEM-HAADF images of Rh-C<sub>60</sub> 1/1 (top) and Rh-C<sub>60</sub> 10/1 (bottom) together with the EDX line scanning profile of Rh signals extracted from cumulated EDX spectra on the line scans (right) (scale bars from left to right: 50 nm, 50 nm, 10 nm and 50 nm).

analyses carried out for the Rh-C<sub>60</sub> 10/1 sample, for which the Rh NPs on the surface were more abundant (Fig. 2). In addition, the distribution of the Rh signal by EDX analysis along the line scan is uniform for sample 1/1 (Fig. 2) while this confirms the presence of Rh NPs on the surface of Rh-C<sub>60</sub> 10/1, as a higher Rh content was detected on the surface of the sphere. ICP analyses pointed out that the rhodium content was lower than expected, which suggested the presence of residual DCB on the samples, further corroborated by IR, SSNMR and TGA, as detailed below.

In order to obtain more insight into the evolution of these Rh-C<sub>60</sub> species during the synthesis, the reaction was monitored by *ex situ* TEM analyses. For that, the decomposition of [Rh( $\eta^3$ -C<sub>3</sub>H<sub>5</sub>)<sub>3</sub>] under hydrogen in the presence of fullerene C<sub>60</sub> (Rh/C<sub>60</sub> = 10/1) was performed at low temperature (−20 °C). The reaction mixture was sampled over time and the TEM images are displayed in Fig. S2† together with their respective size histograms. The evolution of the nanostructures over time showed that at 2 min of reaction, worm-like structures composed of nanospheres were already formed, with a nanosphere mean size of 218.7 ± 23.9 nm, which evolved to independent nanospheres after 5 min of reaction displaying a larger mean size, 274.4 ± 33.1 nm (Table S1†). Rh nanoparticles were observed after 15 min of reaction on the surface of the nanospheres and dispersed on the TEM grid, 1.7 ± 0.5 and 3.4 ± 1.3 nm, respectively. The

reaction was allowed to proceed overnight at −20 °C and the last TEM analysis performed showed that the size of the nanospheres remained similar, 255.7 ± 39.5 nm, while the Rh NPs on the surface presented a bimodal distribution, 2.4 ± 0.7 and 4.7 ± 0.4 nm and isolated NPs were no longer observed. These observations make it feasible to propose that, as previously observed during the synthesis of Ru-C<sub>60</sub> compounds,<sup>30</sup> the nanospheres are composed of molecular species, which form this particular shape due to the stirring and the different viscosities between the as-synthesized species and the solvent.<sup>40</sup> For the previously described Ru-C<sub>60</sub> species, lower solvent viscosity leads to smaller nanospheres. Here, the decrease of the temperature to −20 °C increased the size of the nanospheres when compared to the synthesis performed at 50 °C (255.7 ± 39.5 nm for −20 °C, 103.0 ± 15.5 nm for 50 °C). Taking into account that the viscosity increases when the temperature decreases, an increase of the diameter is expected, as observed here. Also, the detection of isolated NPs at 15 min could indicate that double NP nucleation occurs during the synthesis: one on the surface of the Rh-C<sub>60</sub> nanospheres and a second one in solution. It is possible that the rhodium precursor reacts with the solvent, as arene-rhodium complexes have been described in the past.<sup>41–43</sup> The arene ring of DCB, being electro-deficient, should coordinate weakly when compared to other arene compounds such as benzene or toluene,<sup>43</sup>



producing also NPs under reaction conditions. In addition, the fact that the Rh NPs are stabilized by a weakly stabilizing ligand (DCB) could also explain that the isolated NPs observed first are then adsorbed on the surface of the nanospheres, explaining in turn the bimodal size distributions and the polydispersity (around 30%) of the samples.

WAXS analyses were performed on the Rh nanostructures. After corrections and Fourier transform, the radial distribution function was obtained (RDF, Fig. S3†). For the lowest Rh amounts (*i.e.* 1/1 and 2/1), the observed RDFs present only weak features actually dominated by the distances in C<sub>60</sub>. From 5/1, the distances are consistent with metallic Rh in the fcc structure and both amplitude and coherence length increase in relation to the Rh amount. Coherence lengths could be estimated to be 3.3 nm for 5/1, 3.5 nm for 10/1 and 3.8 nm for 20/1. It should be noted that the scattering phenomenon strongly emphasizes the contribution of larger particles, which does not make it very sensitive to size distribution. This behaviour has been previously observed for Ru-C<sub>60</sub> species.<sup>30</sup>

To gain further insight into the interactions between Rh and fullerene, XPS analyses of Rh-C<sub>60</sub> 1/1 and 10/1 were conducted (Fig. 3 and S4 and Table S2†). Peaks in the full XPS spectra indicate the presence of Rh, C and O elements on both samples (Fig. S4†). Rh 3d peaks could be fitted into a unimodal doublet, pointing to the presence of only one Rh chemical state: metallic Rh<sup>0</sup>. In the Rh 3d region of the Rh-C<sub>60</sub> 1/1 XPS spectrum, a single doublet is observed at 307.8 eV (3d<sub>5/2</sub>) and 312.4 eV (3d<sub>3/2</sub>). These binding energies may evidence charge transfer from the metal to the C<sub>60</sub> molecules, since they are significantly shifted compared to that of metallic rhodium (Rh 3d<sub>5/2</sub> component at 307.2 eV).<sup>44</sup> The Rh 3d core peaks of Rh-C<sub>60</sub> 10/1 are asymmetric and appear at relatively lower binding energies *i.e.* 307.2 eV (3d<sub>5/2</sub>) and 311.9 eV (3d<sub>3/2</sub>), which are typical of metallic Rh<sup>0</sup>. Such an asymmetry could be explained by the presence of a second contribution at slightly higher binding energies, consistent with the charge transfer mentioned above. In agreement with

the EDX results presented earlier, the atomic percentage (Table S2†) for rhodium is higher for Rh-C<sub>60</sub> 10/1 (8.0%) than that for Rh-C<sub>60</sub> 1/1 (1.5%). For both samples, the C 1s peaks (Fig. S4 and Table S2†) are dominated by a peak at 284.3 eV attributed to fullerene C<sub>60</sub>, with less intense peaks associated with contaminating carbon (285.0 eV), oxygenated carbon groups (between 286 and 288.5 eV) and a shake-up peak (at *ca.* 290.0 eV). It is to be noted that the binding energy of 284.3 eV is significantly lower than the value reported for the C 1s peak of fullerene films thicker than one monolayer (approximately 284.8 eV).<sup>45</sup> This shift is consistent with the charge transfer mentioned above, as observed for a 1-monolayer-thick film of C<sub>60</sub> on Cu(111).<sup>45</sup> The O 1s peaks (Fig. S4 and Table S2†) for both samples correspond to oxygen atoms bound to carbon.

Raman spectroscopy is an efficient technique to study C<sub>60</sub> as it can provide important information on various vibrational modes, and thereby one can understand the crystallinity, structure, intramolecular bond formation and molecular deformation. The C<sub>60</sub> molecule has 46 intramolecular modes, among which 10 are Raman active (2 Ag + 8 Hg). The Ag (1) mode at ~492 cm<sup>-1</sup> is known as the breathing mode, which originates from the in phase radial movement of all sixty carbon atoms in the icosahedral structure. The second Ag mode Ag (2), situated at 1458–1468 cm<sup>-1</sup>, is also known as the pentagonal pinch mode corresponding to the in phase tangential displacement of carbon atoms, leading to an out of phase breathing mode of pentagon and hexagon faces. Similarly, the low frequency Hg modes (<700 cm<sup>-1</sup>) mainly arise from the radial molecular movement, whereas higher frequency Hg modes are mainly due to the tangential displacements.<sup>46,47</sup> The Raman spectrum of C<sub>60</sub> displays intense tangential Raman modes of vibrations such as Ag (2), Hg (7), and Hg (8) at 1459 cm<sup>-1</sup>, 1429 cm<sup>-1</sup>, and 1561 cm<sup>-1</sup> respectively. Fig. 4 shows the Raman spectra of Rh-C<sub>60</sub> samples with different Rh/C<sub>60</sub> ratios and Table 2 lists the peak position, peak shift and full width at half maximum (FWHM) as a function of the Rh/C<sub>60</sub> ratios, which are obtained by peak fitting using the Lorentzian function. It is observed that after Rh introduction, the peaks are broadened with a decrease in intensity as well as an increase in luminescence background. The Ag (2) and Hg (7) peaks show downshifts, whereas Hg (8) shows an upshift as compared to the corresponding C<sub>60</sub> peak positions. The FWHM values of the rhodium containing samples are considerably larger compared to that of the C<sub>60</sub> fullerene. For the Rh-C<sub>60</sub> samples, the low frequency vibrations are not clearly visible because of a large luminescence background and the softening of these modes. The shifts in the tangential modes at a higher wavenumber have been assigned in the literature to the electron transfer from dopants to the C<sub>60</sub> molecule.<sup>48</sup> The broadening of these prominent modes, mainly those of Hg (7) and Hg (8), are explained by the electron-phonon coupling due to doping. The broadening of the Ag (2) mode is explained by the expansion of the C<sub>60</sub> molecule, which reduces the force constants.<sup>48</sup> The reported

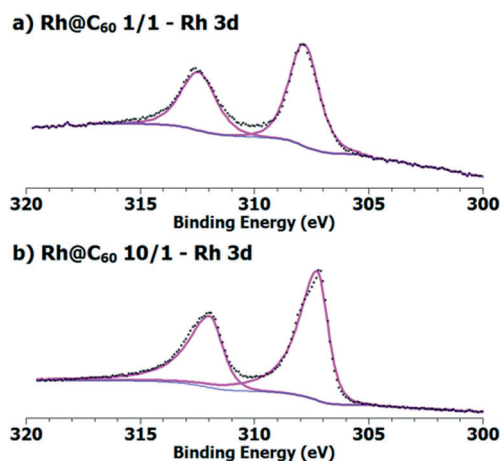


Fig. 3 XPS Rh 3d spectra of a) Rh-C<sub>60</sub> 1/1 and b) Rh-C<sub>60</sub> 10/1.

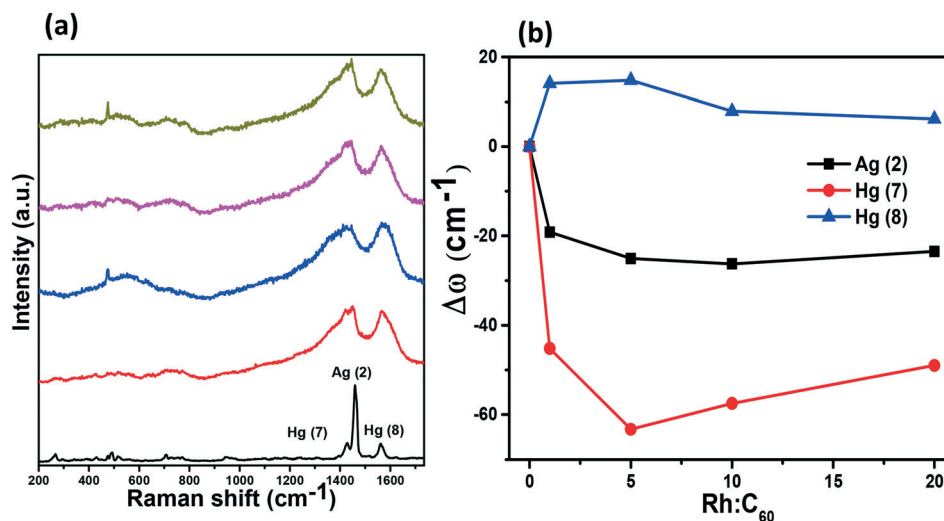


Fig. 4 a) Raman spectra of  $C_{60}$  fullerene together with Rh- $C_{60}$  nanostructures and b) shift in peak position vs. Rh/ $C_{60}$  ratio.

Table 2 Peak position, shift of peaks and FWHM of  $C_{60}$  and Rh- $C_{60}$

	Ag (2)			Hg (7)			Hg (8)		
	Position ( $\text{cm}^{-1}$ )	Shift ( $\text{cm}^{-1}$ )	FWHM	Position ( $\text{cm}^{-1}$ )	Shift ( $\text{cm}^{-1}$ )	FWHM	Position ( $\text{cm}^{-1}$ )	Shift ( $\text{cm}^{-1}$ )	FWHM
$C_{60}$	1459.1	0	15.1	1423.6	0	17.2	1563.2	0	20.1
Rh- $C_{60}$ 1/1	1439.9	-19.2	65	1378.4	-45.2	206.4	1577.3	14.1	84.6
Rh- $C_{60}$ 5/1	1434.0	-25.1	105.6	1360.3	-63.3	181.5	1578.0	14.8	81.2
Rh- $C_{60}$ 10/1	1432.8	-26.3	71	1366.1	-57.5	267.1	1571.1	7.9	82.85
Rh- $C_{60}$ 20/1	1435.6	-23.5	61.1	1374.6	-49	239.8	1569.4	6.2	77

electron transfer for the downshift of tangential modes of vibrations at a higher wavelength are  $-6 \text{ cm}^{-1}$  per electron for Ag (2),  $-7 \text{ cm}^{-1}$  per electron for Hg (7) and  $-15 \text{ cm}^{-1}$  per electron for Hg (8).<sup>49</sup> The downshift of the pentagonal pinch mode is commonly used to quantify the charge transfer from the metal to the antibonding electron orbitals of the  $C_{60}$  molecule since it is the most intense peak in the Raman spectra of  $C_{60}$ . Meanwhile, Rh- $C_{60}$  10/1 shows a higher downshift of  $-26.3 \text{ cm}^{-1}$  corresponding to an electron transfer of  $\sim 4.4 e^-$  and Rh- $C_{60}$  20/1 exhibits a downshift of  $-23.5 \text{ cm}^{-1}$  corresponding to an electron transfer of  $\sim 3.9 e^-$ . For Rh doping, the negative shift and broadening increases for up to 10/1, but decreases for 20/1, and from this, we can predict that there is saturation with respect to Rh doping.

The ATR-IR spectra of the Rh- $C_{60}$  nanostructures were recorded in the solid state (Fig. S5-a†). Characteristic peaks of fullerene  $C_{60}$  are observed at 518, 577, and  $1182 \text{ cm}^{-1}$ , which confirm the presence of the stabilizing molecules in the samples. Other intense peaks are attributed to the presence of DCB (657, 745, 1033, 1124, 1432 and  $1454 \text{ cm}^{-1}$ ). The SSNMR of Rh- $C_{60}$  10/1 (Fig. S6†) confirmed the presence of fullerene  $C_{60}$ , whose signal appears at 147.1 ppm. The MAS  $^{13}\text{C}\{^1\text{H}\}$  NMR also show two signals at 130.9 and 128.1 ppm, which were attributed to remaining DCB and corroborated the presence of the solvent in the samples as seen in the ATR-IR spectra. The CP-MAS  $^{13}\text{C}$  NMR (CP =  $^1\text{H}$ - $^{13}\text{C}$  cross polarization) allowed the observation of a broad

signal centered around 43 ppm attributed to a mixture of hydrogenated fullerene species. The hydrogenation of fullerene  $C_{60}$  at ambient temperature and pressure has already been reported for the Rh/ $\text{Al}_2\text{O}_3$  catalyst,<sup>50</sup> and the formation of these hydrogenated species were also observed for Ru- $C_{60}$  materials.<sup>30</sup> Adsorbed DCB was removed by annealing the samples at  $200^\circ\text{C}$  under Ar. The ATR-IR spectra (Fig. S5-b†) recorded for the heat-treated samples show that the DCB peaks vanished. Additionally, TGA analyses (Fig. S7†) confirmed the efficiency of the thermal treatment. No appreciable structural change of the nanospheres was observed from TEM analyses on the Rh- $C_{60}$  5/1 sample (denoted as Rh- $C_{60}$  5/1 TT) (Fig. S8†); however, the size distribution of the NPs was unimodal, centred at  $1.8 \pm 0.5 \text{ nm}$ , which could be attributed to slight sintering of the small nanoparticles.

To evaluate the catalytic performance of the Rh- $C_{60}$  catalysts, we selected the quinoline hydrogenation, as rhodium based catalysts have shown very good performances in this reaction (Scheme 1 and Tables 3 and 4).<sup>20,22,24</sup> In addition, the fact that Rh is electron deficient, as evidenced by Raman and XPS, can be an advantage to obtain higher selectivity, as Rh-NHC carbene species,<sup>24</sup> bearing strong donating groups on the Rh NP surface, are very active for this reduction reaction working at  $30^\circ\text{C}$  but not very selective to the synthesis of 2. Theoretical calculations supported our first analysis, as Rh-based catalysts intrinsically coordinate

**Table 3** Selective hydrogenation of quinoline using the Rh-C<sub>60</sub> 10/1 nanocatalyst<sup>a</sup>

Entry	T (°C)	Solvent	TOF <sup>b</sup> (h <sup>-1</sup> )	Time (h)	Conversion <sup>b,c</sup> (%)	Selectivity <sup>c</sup> (%)		
						2	3	4
1	60	THF	19.5	1	7	100	—	—
2				4	44	98	1	1
3	80	THF	47.8	1	38	97	1	2
4				4	65	97	1	2
5	100	THF	118.6	1	75	98	1	1
6				4	100	97	1	2
7	100	Toluene	99.8	1	57	97	1	2
8				4	90	98	1	1
9	100	Isopropanol	123.4	1	78	98	1	1
10				4	99	97	1	2

<sup>a</sup> Reaction conditions: 0.02 mmol Rh, 404 mg (3.1 mmol) of quinoline, 75 mg (0.41 mmol) of dodecane (internal standard), 20 bar H<sub>2</sub>, 25 ml of solvent. <sup>b</sup> TOFs calculated at 1 h of reaction related to the % of Rh. <sup>c</sup> Conversion and selectivity determined by GC analyses using the internal standard technique.

**Table 4** Selective hydrogenation of quinoline using the Rh-C<sub>60</sub> nanocatalyst<sup>a</sup>

Entry	Catalyst	TOF <sup>b</sup> (h <sup>-1</sup> )	Time (h)	Conversion <sup>b,c</sup> (%)	Selectivity <sup>c</sup> (%)		
					2	3	4
1	Rh-C <sub>60</sub> 1/1	94.3	1	54	100	—	—
2			4	80	100	—	—
3	Rh-C <sub>60</sub> 5/1	164.3	1	98	96	1	3
4			4	99	94	1	5
5	Rh-C <sub>60</sub> 5/1 TT	157.1	1	99	97	1	3
6	Rh-C <sub>60</sub> 10/1	123.4	1	78	98	1	1
7			4	99	97	1	2
8	Rh-C <sub>60</sub> 20/1	157.7	1	97	92	3	5
9			4	99	90	3	7

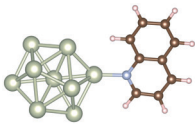
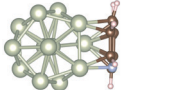
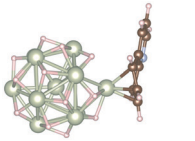
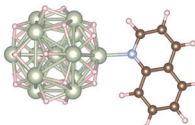
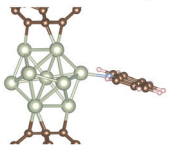
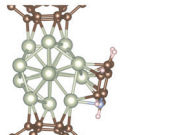
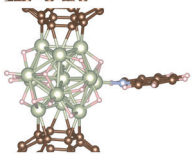
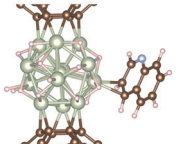
<sup>a</sup> Reaction conditions: 0.02 mmol Rh, 404 mg (3.1 mmol) of quinoline, 75 mg (0.41 mmol) of dodecane (internal standard), 100 °C, 20 bar H<sub>2</sub>, 25 ml of solvent. <sup>b</sup> TOFs calculated at 1 h of reaction related to the % of Rh. <sup>c</sup> Conversion and selectivity determined by GC analyses using the internal standard technique.

the N-bearing ring more efficiently (Table 5, Rh<sub>13</sub>H<sub>20</sub> N vs. aromatic ring coordination), therefore, giving preferentially the partially hydrogenated product 2, as observed in most of the reviewed reported studies. Concerning the coordination of 1,2,3,4-tetrahydroquinoline (2) to rhodium clusters, this difference is less pronounced (Table 6, Rh<sub>13</sub>H<sub>20</sub> N vs. aromatic ring coordination), as both coordination modes are possible with similar adsorption energies (*E*<sub>ads</sub>) and *a priori* the coordination of the aromatic group could lead to the complete hydrogenation of the molecule. As this is not so usual in the existing literature, probably steric effects should be taken into consideration, as further coordination of another 2 molecule would give extra stabilization, leading to poisoning of the Rh surface by the product, an argument which is pointed out in some cases to explain the high selectivity of Rh systems.<sup>24</sup> We recall that full hydrogenation is possible too.<sup>51,52</sup> The present DFT study also supported our hypothesis that the use of Rh electron deficient species should be an advantage to obtain higher selectivity. Indeed, by comparing the coordination of quinoline to systems, such as Rh<sub>13</sub>H<sub>20</sub> (to mimic bare Rh NPs under hydrogenation conditions) and C<sub>60</sub>-Rh<sub>13</sub>H<sub>20</sub>-C<sub>60</sub> (Table 5), it is observed that the hydrogenated Rh NPs interacting with fullerenes can

coordinate the N-bearing aromatic ring in two distinct modes (by N or by two carbon bonds) with a similar *E*<sub>ads</sub>. This is in contrast with the coordination of quinoline to Rh<sub>13</sub>H<sub>20</sub>, in which the coordination of the N atom is largely favourable. This could explain the high TOF observed in the hydrogenation of quinoline using Rh-C<sub>60</sub> as a catalyst discussed below. The analyses of the coordination of compound 2 to the C<sub>60</sub>-Rh<sub>13</sub>H<sub>20</sub>-C<sub>60</sub> system (Table 6), in comparison with Rh<sub>13</sub>H<sub>20</sub>, show that in this case, only the coordination by the N atom is possible, in contrast with Rh<sub>13</sub>H<sub>20</sub> for which two coordinating modes close in adsorption energies are possible. This observation, the strong coordination of the partially hydrogenated product, could explain the high selectivity of Rh-C<sub>60</sub>.

Experimentally, Rh-C<sub>60</sub> catalysts were active and highly selective for the hydrogenation of the pyridine ring of quinoline (Tables 3 and 4). Using the best conditions, the selectivity towards 1,2,3,4-tetrahydroquinoline (2) at full conversion was in the range of 92–98% for all catalysts. The Rh-C<sub>60</sub> 10/1 catalyst was used to optimise the reaction conditions (Table 3). As expected, the catalytic activity increased with the temperature, and the conversion of quinoline at 4 h of reaction was 44%, 65% and 100% at 60

**Table 5** DFT results of quinoline adsorption on several Rh<sub>13</sub> clusters; comparisons between adsorption modes (N vs. aromatic ring) are highlighted and charge transfer<sup>a</sup> is given

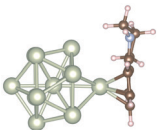
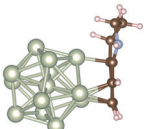
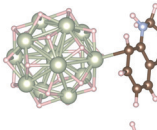
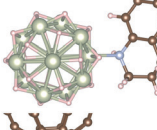
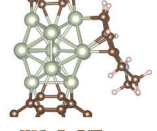
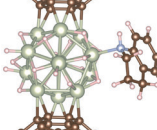
Support	Adsorption mode	$E_{\text{ads}}$ (kcal mol <sup>-1</sup> )	Charge transfer (e <sup>-</sup> )
Rh <sub>13</sub>		-24	+0.01
		-64	+0.40
Rh <sub>13</sub> H <sub>20</sub>		-9	-0.01
		-25	-0.10
C <sub>60</sub> -Rh <sub>13</sub> -C <sub>60</sub>		-25	-0.09
		-59	+0.24
C <sub>60</sub> -Rh <sub>13</sub> H <sub>20</sub> -C <sub>60</sub>		-26	-0.14
		-33	+0.03

<sup>a</sup> Positive charge transfer means that the substrate receives electronic density from the support.

°C, 80 °C and 100 °C, respectively. The catalytic activity was also sensitive to the solvent, and the conversion of quinoline increased, following the order toluene < THF ≤ isopropanol, which is in agreement with previous studies where highly polar solvents are more efficient in hydrogenation reactions with regard to low-polarity ones.<sup>53–56</sup> The reactions performed at 100 °C reached full conversion at 3 h of reaction when using isopropanol or THF as a solvent and 7 h in the case of toluene, with high selectivity to 2, 97%, 97% and 95%, respectively. Reactions carried out in isopropanol and toluene were allowed to react for longer times in order to produce the fully hydrogenated product. Nevertheless, after 24 h of reaction, the composition of the reaction mixture was very similar; for toluene, the selectivity towards 2 at 7 h (full

conversion) and 24 h was the same (97%), while for isopropanol, a slight increase of the selectivity to fully hydrogenated compound 4 was observed, from 1% at 3 h to 5% at 24 h. Time-concentration curves for the quinoline hydrogenation with Rh-C<sub>60</sub> 10/1 in toluene and isopropanol are shown in Fig. S9 and S10,<sup>†</sup> respectively. The high selectivity of Rh-C<sub>60</sub> towards 2 is independent of the solvent used, which is in contrast with some reported systems in which the selectivity is sensitive to the solvent.<sup>26,57</sup> Additionally, the hydrogenation of 2 and 5,6,7,8-tetrahydroquinoline (3) were evaluated in independent catalytic tests using Rh-C<sub>60</sub> 10/1 as the catalyst in isopropanol. The hydrogenation of 2 was very slow (TOF = 4.8 h<sup>-1</sup>), reaching a conversion of 11% at 5 h, which remained

**Table 6** DFT results of 1,2,3,4-tetrahydroquinoline adsorption on various supports; comparisons between adsorption modes (N vs. aromatic ring) are highlighted and charge transfer<sup>a</sup> is given

Support	Adsorption mode	$E_{\text{ads}}$ (kcal mol <sup>-1</sup> )	Charge transfer (e <sup>-</sup> )
Rh <sub>13</sub>		-27	-0.08
		-54	+0.10
Rh <sub>13</sub> H <sub>20</sub>		-17	-0.19
		-18	-0.13
C <sub>60</sub> -Rh <sub>13</sub> -C <sub>60</sub>		-64	-0.08
		-20	-0.23

<sup>a</sup> Positive charge transfer means that the substrate receives electronic density from the support.

almost unchanged at 24 h of reaction (13% conversion). On the other hand, the hydrogenation of **3** was slightly more efficient (TOF = 23.1 h<sup>-1</sup>), displaying 15% conversion at 5 h and 26% conversion at 24 h of reaction.

The Rh-C<sub>60</sub> series was tested as catalysts in the hydrogenation of quinoline under the optimized conditions, *i.e.* using isopropanol as the solvent at 100 °C under 20 bar of H<sub>2</sub> pressure (Table 4). The time-concentration curves for the quinoline hydrogenation with the Rh-C<sub>60</sub> series are shown in Fig. S11.† In all cases, except for Rh-C<sub>60</sub> 1/1, full conversion of quinoline was achieved within an hour, with high selectivity towards **2** (92–98%). The TOFs were very similar among them, indicating that the concentration of rhodium has no effect on both activity and selectivity. This result is in line with Raman analyses, in which similar charge transfer was evidenced for samples 5/1 to 20/1. In contrast, the Rh-C<sub>60</sub> 1/1 catalyst displayed the lowest activity in the series, and it is probably because only a few nanoparticles are available on the surface of the nanospheres as ascertained by HRTEM analyses. The TEM analyses of the catalysts after the hydrogenation reaction showed that the nanospheres remained almost unchanged except for Rh-C<sub>60</sub> 1/1 where two populations of sizes centred at 75.0 ± 23.6 and

364.2 ± 27.8 nm (Fig. S13†) were observed (the mean size distribution of the as-synthesised compound was 158.2 ± 27.5 nm), indicating that these molecular species can evolve under the catalytic reaction conditions. Also, the Rh NP mean size distribution for Rh-C<sub>60</sub> 5/1 and Rh-C<sub>60</sub> 10/1 changed, displaying a monomodal distribution but is very polydisperse (Fig. S13†). In addition, a few isolated NPs were observed in the TEM grid on the Rh-C<sub>60</sub> 10/1 sample, indicating that the Rh NPs are not stable on the nanosphere surface during catalysis.

At first sight, no remarkable effect of the thermal treatment (TT), performed to remove adsorbed DCB, was noticed for sample Rh-C<sub>60</sub> 5/1 *vs.* Rh-C<sub>60</sub> 5/1 TT (Table 4, entry 3 *vs.* entry 5), although it is difficult to compare as the reaction was complete within one hour. The catalytic performances of both catalysts, Rh-C<sub>60</sub> 5/1 and Rh-C<sub>60</sub> 5/1 TT, were compared at a lower temperature, 80 °C, using smaller time intervals to analyze the reaction mixtures. Under these conditions, Rh-C<sub>60</sub> 5/1 TT showed a higher TOF at 15 minutes of reaction, 302.2 h<sup>-1</sup>, than Rh-C<sub>60</sub> 5/1, 253.8 h<sup>-1</sup>. Quinoline was completely consumed within 1 h and 1.5 h, respectively. When the reaction was performed at 100 °C using Rh-C<sub>60</sub> 5/1 TT as the catalyst, the quinoline conversion



was 94% at 15 min, reaching full conversion within 30 min (98% selectivity towards 2), thus the calculated TOF at 15 min is  $488.0 \text{ h}^{-1}$ , which is as high as those of some other representative heterogeneous catalysts (Table S3†).<sup>17,22–24,27–29,58</sup>

The recycling of the catalysts was investigated using Rh-C<sub>60</sub> 5/1 and Rh-C<sub>60</sub> 5/1 TT due to their higher activity and selectivity when compared to the rest of the series (Fig. 5).

Rh-C<sub>60</sub> 5/1 could be reused three times without a loss of catalytic activity; nevertheless, at the fourth recycling, the conversion dropped to 70%. On the other hand, Rh-C<sub>60</sub> 5/1 TT was revealed to be more robust and was recycled five times without a loss of catalytic activity. Also, TEM analyses of the Rh-C<sub>60</sub> TT 5/1 catalyst after the recycling test showed no appreciable change in the nanosphere size while the Rh NP mean size increased to  $2.7 \pm 0.7 \text{ nm}$ .

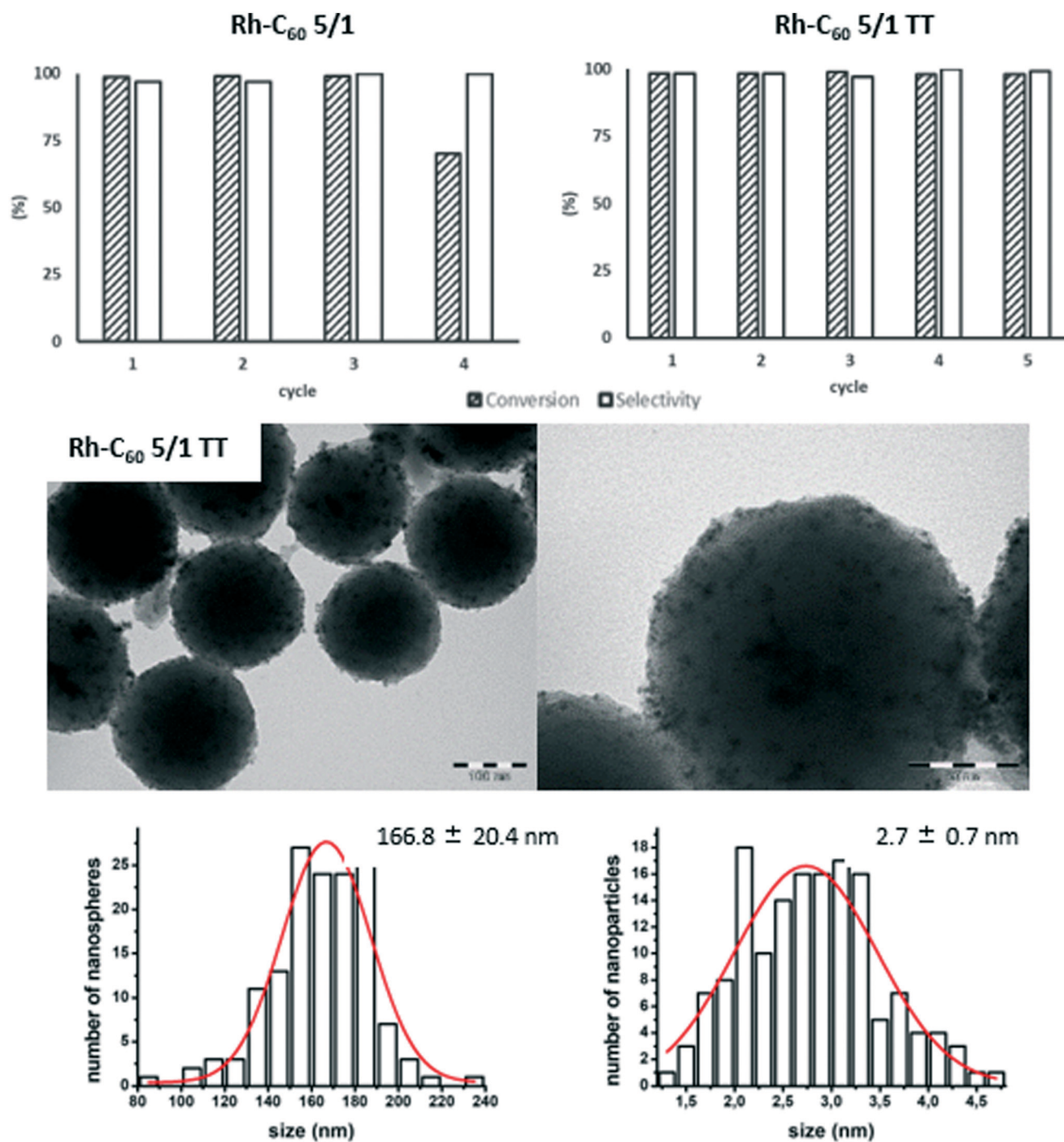


Fig. 5 Conversion and selectivity after the recycling tests using Rh-C<sub>60</sub> 5/1 and Rh-C<sub>60</sub> 5/1 TT together with the TEM images and size distribution histograms of Rh-C<sub>60</sub> 5/1 TT after the recycling test (scale bar from left to right: 100 nm and 50 nm).

A DFT study has been performed in order to explore the coordination thermodynamics of quinoline (1) and 1,2,3,4-tetrahydroquinoline (2) on several  $\text{Rh}_{13}$  molecular models (Tables 5 and 6). The four molecular models, denoted as supports in the tables, included a bare  $\text{Rh}_{13}$  cluster, a hydride covered  $\text{Rh}_{13}$  cluster ( $\text{Rh}_{13}\text{H}_{20}$ ), and the analogous systems with two coordinated fullerene  $\text{C}_{60}$  onto the Rh surface ( $\text{C}_{60}\text{-Rh}_{13}\text{-C}_{60}$  and  $\text{C}_{60}\text{-Rh}_{13}\text{H}_{20}\text{-C}_{60}$ ). A coverage value of 1.7 H atom per surface Rh atom was slightly higher than the value previously used by us for Ru systems (1.5 H in  $\text{Ru}_{13}\text{H}_{18}$ ),<sup>31,32</sup> since one can assume that extra hydrides with small adsorption energies are probably involved in the hydrogenation reactions. Hydrogenated Rh NP models simulate the surface of the NPs under hydrogenation conditions.<sup>59</sup> The use of two fullerene  $\text{C}_{60}$  was chosen by analogy to our previous DFT calculations on Ru- $\text{C}_{60}$  systems.<sup>31,32</sup> The adsorption energies and charge transfer of compounds 1 and 2 on those models are given after carefully checking the nature of the most stable geometries. The presence of the surface hydrides highly influences the coordination mode and the adsorption energy in both compounds. The bare  $\text{Rh}_{13}$  cluster very efficiently coordinates quinoline through  $\pi$ -coordination of the N-bearing aryl ring ( $-64 \text{ kcal mol}^{-1}$   $\text{Rh}_{13}\text{-1}$ , Table 5), while  $\text{Rh}_{13}\text{H}_{20}$  prefers to coordinate through the N atom ( $-25 \text{ kcal mol}^{-1}$   $\text{Rh}_{13}\text{H}_{20}\text{-1}$ , Table 5) and  $\pi$ -coordination is calculated to be very unfavourable, but possible ( $-9 \text{ kcal mol}^{-1}$   $\text{Rh}_{13}\text{H}_{20}\text{-1}$ , Table 5). Similarly, the coordination mode of 2 over  $\text{Rh}_{13}$  and  $\text{Rh}_{13}\text{H}_{20}$  is largely influenced by the surface hydrides. While the bare  $\text{Rh}_{13}$  cluster accommodates compound 2 in a very stable way through  $\pi$ -coordination of the aryl ring ( $-54 \text{ kcal mol}^{-1}$   $\text{Rh}_{13}\text{-2}$ , Table 6) after the addition of hydrides onto the Rh surface, this coordination is not possible leading to coordination through the N atom ( $-18 \text{ kcal mol}^{-1}$   $\text{Rh}_{13}\text{H}_{20}\text{-2}$ , Table 6) or through the coordination of two C atoms of the aryl ring in the  $\eta^2$  position with Rh-C distances of 2.27 and 2.42 Å, which is very close in adsorption energy ( $-17 \text{ kcal mol}^{-1}$   $\text{Rh}_{13}\text{H}_{20}\text{-2}$ , Table 6).

Likewise, this phenomenon is also observed in the adsorption of compound 2 on  $\text{Rh}_{13}$  clusters bearing fullerene  $\text{C}_{60}$  on their surface ( $\pi$ -coordination on  $\text{C}_{60}\text{-Rh}_{13}\text{-C}_{60}$  ( $-64 \text{ kcal mol}^{-1}$   $\text{C}_{60}\text{-Rh}_{13}\text{-C}_{60}\text{-2}$ , Table 6) vs. N-coordination on  $\text{C}_{60}\text{-Rh}_{13}\text{H}_{20}\text{-C}_{60}$  ( $-20 \text{ kcal mol}^{-1}$   $\text{C}_{60}\text{-Rh}_{13}\text{H}_{20}\text{-C}_{60}\text{-2}$ , Table 6)). The coordination of quinoline 1 on  $\text{C}_{60}\text{-Rh}_{13}\text{H}_{20}\text{-C}_{60}$  followed a slightly different trend. Even if similar,  $\pi$ -coordination is not possible over the hydrogenated cluster in contrast with the highly stable  $\pi$ -coordination observed on  $\text{C}_{60}\text{-Rh}_{13}\text{-C}_{60}$  ( $-59 \text{ kcal mol}^{-1}$   $\text{C}_{60}\text{-Rh}_{13}\text{-C}_{60}\text{-1}$ , Table 5) and N-coordination of 1 is favourable over  $\text{C}_{60}\text{-Rh}_{13}\text{H}_{20}\text{-C}_{60}$  ( $-26 \text{ kcal mol}^{-1}$   $\text{C}_{60}\text{-Rh}_{13}\text{H}_{20}\text{-C}_{60}\text{-1}$ , Table 5); the coordination of two carbon atoms of the N-aryl ring to one rhodium atom displays a more stable adsorption energy ( $-33 \text{ kcal mol}^{-1}$   $\text{C}_{60}\text{-Rh}_{13}\text{H}_{20}\text{-C}_{60}\text{-1}$ , Table 5). As a general trend for these calculations, the hydride coverage changes the coordination mode stability. Highly stable  $\pi$ -coordination is observed on bare  $\text{Rh}_{13}$  clusters, whereas at high coverage ( $\text{Rh}_{13}\text{H}_{20}$ ), N-coordination prevails.

The effect of the hydride coverage could be attributed to two factors, first, they pull electronic densities from Rh atoms and their presence on the surface impedes the  $\pi$ -coordination through steric effects. This effect has been already observed by us in previous studies dealing with Ru NPs.<sup>31,32</sup>

The hydride coverage governs the coordination mode of the substrate and the partially hydrogenated product to the Rh surface; nevertheless, whether fullerene  $\text{C}_{60}$  on the surface is present or not, it also modulates the stability of the adsorbed species. In general, the addition of fullerene  $\text{C}_{60}$  decreased the charge transfer, as experimentally observed. Quinoline prefers to coordinate to the surface through a  $\pi$ -coordination mode of the N-bearing aryl ring in bare  $\text{Rh}_{13}$  and  $\text{C}_{60}\text{-Rh}_{13}\text{-C}_{60}$ , with a slight decrease of the adsorption energy and a change in the charge transfer (Table 5,  $-64 \text{ kcal mol}^{-1} + 0.40 \text{ e}^-$  vs.  $-59 \text{ kcal mol}^{-1} + 0.24 \text{ e}^-$ , respectively). Likewise, the coordination of compound 2 on bare  $\text{Rh}_{13}$  and  $\text{C}_{60}\text{-Rh}_{13}\text{-C}_{60}$  displayed a similar trend, but the  $\pi$ -coordination on  $\text{C}_{60}\text{-Rh}_{13}\text{-C}_{60}$  was found to be more stable (Table 6,  $-54 \text{ kcal mol}^{-1} + 0.10 \text{ e}^-$  ( $\text{Rh}_{13}$ ) vs.  $-64 \text{ kcal mol}^{-1} - 0.08 \text{ e}^-$  ( $\text{C}_{60}\text{-Rh}_{13}\text{-C}_{60}$ )). The comparison of the effect of the fullerene  $\text{C}_{60}$  coordination on hydrogenated clusters supports the trends observed experimentally, *i.e.* the enhanced activity observed with the presence of fullerene  $\text{C}_{60}$  on the surface compared to other reported systems. Quinoline coordinates to the surface of  $\text{Rh}_{13}\text{H}_{20}$  and  $\text{C}_{60}\text{-Rh}_{13}\text{H}_{20}\text{-C}_{60}$  through the N-atom displaying similar adsorption energies ( $-25 \text{ kcal mol}^{-1}$  vs.  $-26 \text{ kcal mol}^{-1}$ , Table 5), but the presence of fullerene  $\text{C}_{60}$  allowed the coordination of quinoline through the two carbon atoms of the N-aryl ring in a more stable way ( $-33 \text{ kcal mol}^{-1}$ , Table 5), which could explain the higher activity of Rh- $\text{C}_{60}$  compared to those of other reported systems (see Table S3†). Also,  $\text{C}_{60}\text{-Rh}_{13}\text{H}_{20}\text{-C}_{60}$  accommodates compound 2 through the N-atom in a more stable manner compared to  $\text{Rh}_{13}\text{H}_{20}$ , which could explain that the Rh- $\text{C}_{60}$  system is highly selective. This is also supported by the fact that the coordination through the aromatic ring was found to be not possible in contrast with  $\text{Rh}_{13}\text{H}_{20}$ . It is also noteworthy to point out that the product 2 did not poison the system for the hydrogenation of quinoline, as quinoline is coordinated more efficiently than 2 to hydrogenated rhodium surfaces ( $-33 \text{ kcal mol}^{-1}$   $\text{C}_{60}\text{-Rh}_{13}\text{H}_{20}\text{-C}_{60}\text{-1}$ , Table 5, vs.  $20 \text{ kcal mol}^{-1}$   $\text{C}_{60}\text{-Rh}_{13}\text{H}_{20}\text{-C}_{60}\text{-2}$ , Table 6).

## Conclusions

A series of Rh- $\text{C}_{60}$  catalysts were produced *via* a  $\text{H}_2$  assisted solution synthesis route. Rh atomically dispersed or Rh NPs were prepared by tuning the molar ratio of the Rh precursor and fullerene  $\text{C}_{60}$ . A significant interaction between Rh and  $\text{C}_{60}$  was evidenced by XPS and Raman analyses, which consisted of charge transfer from the metal to fullerene  $\text{C}_{60}$ . These electron-deficient Rh species are excellent catalysts for the selective reduction of quinoline to the partially hydrogenated product with a selectivity of up to 98%. Thermal annealing of the catalyst was highly beneficial to

improve the stability of these species, as seen in the recycling test, and also activity ( $\text{TOF } 488.0 \text{ h}^{-1}$ ), which is in between the most remarkable heterogeneous catalysts for this reaction. In addition, DFT calculations allowed the determination of the origin of the intrinsic selectivity of Rh NP-based systems when applied as catalysts in the hydrogenation of quinoline. The hydride coverage in Rh- $\text{C}_{60}$  systems plays a pivotal role and explains the origin of the high selectivity of fullerene modified Rh NP systems when applied as a catalyst in the hydrogenation of quinoline.

## Experimental section

### General methods

All operations were carried out under an argon atmosphere using standard Schlenk techniques or in a MBraun glove box. Solvents were purified by standard methods or by an MBraun SPS-800 solvent purification system.  $[\text{Rh}(\eta^3\text{-C}_3\text{H}_5)_3]$  was purchased from Nanomeps Toulouse, fullerene  $\text{C}_{60}$  from Bucky USA, and  $\text{H}_2$  from Air Liquide. All these reactants were used as received.

### Synthesis of Rh- $\text{C}_{60}$

In a typical synthesis, the  $[\text{Rh}(\eta^3\text{-C}_3\text{H}_5)_3]$  complex and fullerene  $\text{C}_{60}$  were placed in a Fisher-Porter bottle in a glove box and dissolved in 1,2-dichlorobenzene (DCB). The resulting purple solution was stirred for 30 min at room temperature, pressurized with 3 bar of  $\text{H}_2$  and then placed in a 50 °C oil bath. The solution turned black in a few minutes and was maintained at this temperature under stirring overnight. After cooling down to room temperature, pentane was added to the reaction mixture to precipitate Rh- $\text{C}_{60}$  which was cleaned twice with pentane. The Rh nanoparticles were obtained as a black solid powder after drying under vacuum overnight. For each ratio studied, the quantities of reactants are detailed hereafter:

Rh- $\text{C}_{60}$  1/1: 50 mg (0.22 mmol) of  $[\text{Rh}(\eta^3\text{-C}_3\text{H}_5)_3]$ , 160 mg (0.22 mmol) of fullerene  $\text{C}_{60}$  and 100 mL of DCB. Yield: 160 mg. Rh content: 9.2%.

Rh- $\text{C}_{60}$  5/1: 25 mg (0.11 mmol) of  $[\text{Rh}(\eta^3\text{-C}_3\text{H}_5)_3]$ , 16 mg (0.02 mmol) of fullerene  $\text{C}_{60}$  and 10 mL of DCB. Yield: 20 mg. Rh content: 23.3%.

Rh- $\text{C}_{60}$  10/1: 100 mg (0.44 mmol) of  $[\text{Rh}(\eta^3\text{-C}_3\text{H}_5)_3]$ , 32 mg (0.04 mmol) of fullerene  $\text{C}_{60}$  and 20 mL of DCB. Yield: 100 mg. Rh content: 35.9%.

Rh- $\text{C}_{60}$  20/1: 200 mg (0.86 mmol) of  $[\text{Rh}(\eta^3\text{-C}_3\text{H}_5)_3]$ , 32 mg (0.04 mmol) of fullerene  $\text{C}_{60}$  and 20 mL of DCB. Yield: 75 mg. Rh content: 46.2%.

### Growth mechanism

The reaction was performed at -20 °C following the standard procedure: 50 mg (0.22 mmol) of  $[\text{Rh}(\eta^3\text{-C}_3\text{H}_5)_3]$ , 16 mg (0.02 mmol) of fullerene  $\text{C}_{60}$  and 10 mL of DCB. The reaction was followed by sampling the mixture over time.

### General procedure for the hydrogenation of quinoline

The hydrogenation of quinoline was performed in a 40 ml stainless steel high-pressure batch BR-25 Berghof reactor. Typically, a mixture of Rh- $\text{C}_{60}$  catalysts (0.02 mmol Rh), dodecane (75 mg; 0.44 mmol) and quinoline (404 mg, 3.12 mmol) in 25 ml of the desired solvent was loaded into the autoclave in the glove box. The autoclave was purged three times with  $\text{H}_2$  to remove the inert atmosphere, heated to 100 °C and charged with 20 bar of  $\text{H}_2$ . The stirring rate was fixed at 1500 rpm. Samples of the reaction mixture were taken at different time intervals and analysed by gas chromatography. Quantitative analyses of the reaction mixtures were performed *via* GC using calibration solutions of commercially available products.

### Catalytic recycling tests

A mixture of quinoline (404 mg, 3.10 mmol), dodecane (75 mg, 0.41 mmol), Rh- $\text{C}_{60}$  5/1 catalysts (0.02 mmol Rh) and 25 ml of isopropanol was prepared in the glove box and introduced into the autoclave. The autoclave was purged three times with  $\text{H}_2$ , heated to 100 °C and pressurized with 20 bar of  $\text{H}_2$  during 1 h keeping the stirring rate at 1500 rpm. After the reaction, the catalyst was recovered into a Schlenk tube by filtering with a cannula and washing several times with EtOH under argon, and then dried under vacuum. The catalyst was reused in another five cycles of the hydrogenation reaction following the procedure described above.

### TEM analyses

TEM and HRTEM analyses were performed at the "Centre de microcaractérisation Raimond Castaing, UMS 3623, Toulouse" by using a JEOL JEM 1011 CXT electron microscope operating at 100 kV with a point resolution of 4.5 Å. The high resolution analyses were conducted using a JEOL JEM 2100F equipped with a field emission gun (FEG) operating at 200 kV with a point resolution of 2.3 Å and a JEOL JEM-ARM200F Cold FEG operating at 200 kV with a point resolution of >1.9 Å. The approximation of the particle mean size was established through a manual analysis of enlarged micrographs by measuring at least 200 particles on a given grid. Other TEM micrographs were acquired with a JEOL 2100F S/TEM microscope equipped with a FEG operating at 200 kV, a spherical aberration probe corrector and a GATAN Tridiem energy filter. The resolutions attained are 2 Å and 1.1 Å under parallel TEM and scanning STEM modes, respectively. For STEM-HAADF analyses, the spot size was 0.13 nm, the current density was 140 pA, and the camera focal length was 10 cm, corresponding to the inner and outer detection angles of the annular detector of about 60 mrad and 160 mrad.

### WAXS analyses

Wide angle X-ray scattering measurements were performed at CEMES on a diffractometer dedicated to pair distribution



function (PDF) analysis: graphite-monochromatized molybdenum radiation (0.07169 nm), solid-state detection and low background setup. Samples were sealed in Lindemann glass capillaries (diameter of 1 mm) to avoid any oxidation after filling in a glove box. For all samples, data were collected on an extended angular range (129 degrees in 2 theta) with counting times of typically 150 s for each of the 457 data points, thus allowing PDF analysis. Classic corrections (polarization and absorption in cylindrical geometry) were applied before reduction and Fourier transform.

### ICP analyses

The rhodium content was established by inductively coupled plasma optical emission spectroscopy (ICP-OES) performed at the LCC on a Thermo Scientific ICAP 6300 instrument after acid mineralization of the samples.

### Raman analyses

Raman measurements were carried out with a Horiba XPLORA-MV2000 spectrometer. For the measurements, an excitation wavelength of 532 nm and a laser power of 0.084 mW were used. The samples were kept under vacuum and exposed to atmospheric air shortly before measurements.

### XPS analyses

XPS measurements were performed on a Thermo K $\alpha$  spectrometer working at a base pressure of  $5 \times 10^{-9}$  mbar and equipped with a monochromatic Al K $\alpha$  X-ray source (1486.7 eV). The spectra presented here were recorded with a pass energy of 20 eV. The data were processed with CasaXPS using Gaussian–Lorentzian combinations and a Shirley background. Scofield photoionization cross-sections<sup>60</sup> corrected for the transmission function of the analyzer and the analysis depth were used for quantifications.

### ATR-IR

ATR-IR spectra were recorded on a Perkin-Elmer GX2000 spectrometer available in a glove box in the range of 4000–400 cm<sup>-1</sup>.

### SSNMR

Solid state NMR (MAS-NMR) with and without <sup>1</sup>H–<sup>13</sup>C cross polarization (CP) were performed at the LCC on a Bruker Avance 400WB instrument equipped with a 4 mm probe with the sample rotation frequency being set at 12 kHz unless otherwise indicated. Measurements were carried out in a 4 mm ZrO<sub>2</sub> rotor.

### TGA

Thermal analysis under air was performed on a thermobalance Perkin Elmer Diamond TG.

### GC analyses

GC analyses were performed on a PerkinElmer Autosystem GC equipped with an Elite-5MS capillary column (30 m  $\times$  0.25 mm  $\times$  0.25  $\mu$ m). Split (20:1); carrier gas flow: He, 20 ml min<sup>-1</sup>; injector temperature: 250 °C; detector (FID) temperature: 250 °C; oven program: 110 °C (hold 12 min) to 230 °C at 20 °C min<sup>-1</sup> (hold 3 min) for a total run time of 21 min; retention time: dodecane, 5.3 min; 1, 7.0 min; 2, 11.3 min; 3, 6.5 min; 4, 4.4 min.

### Computational details

DFT calculations were performed using the Vienna *ab initio* simulation package VASP,<sup>61–64</sup> based on the full-potential projector augmented wave framework.<sup>65,66</sup> Exchange–correlation effects have been approximated using the spin-polarized version of the PBE functional.<sup>67</sup> A kinetic-energy cutoff of 400 eV was found to be sufficient to achieve a total-energy convergence within several meV, considering the *k*-point sampling in Gamma-point only calculations for isolated molecules and complexes, in conjunction with Gaussian smearing with a width of 0.05 eV. During geometry optimization runs, all the atoms were fully relaxed until forces on individual atoms were smaller than 0.01 eV Å<sup>-1</sup>. Calculation cells for isolated molecules and complexes were (25  $\times$  26  $\times$  27) Å<sup>3</sup> to avoid spurious interactions between periodic images. Figures of the different geometries were produced thanks to the 3D visualization program VESTA.<sup>68</sup> Bader charge analyses were performed using Henkelman's group code.<sup>69</sup> The optimal geometries upon H<sub>2</sub> adsorption were constructed, following the results of ref. 70, *i.e.* all available  $\mu_3$  sites were occupied and then the top sites and, if needed, some bridge sites were used to build the starting geometries.

### Conflicts of interest

There are no conflicts to declare.

### Acknowledgements

This work was supported by the Centre National de la Recherche Scientifique (CNRS), which we gratefully acknowledge. I. C. G. acknowledges the Calcul en Midi-Pyrénées initiative CALMIP (Project p0812) for allocations of computer time as well as GENCI-CINES and GENCI-IDRIS for Grant No. 2018-A006096649.

### References

- 1 R. A. Johnstone, A. H. Wilby and I. D. Entwistle, Heterogeneous catalytic transfer hydrogenation and its relation to other methods for reduction of organic compounds, *Chem. Rev.*, 1985, 85, 129–170.
- 2 H. U. Blaser, C. Malan, B. Pugin, F. Spindler, H. Steiner and M. Studer, Selective hydrogenation for fine chemicals: recent trends and new developments, *Adv. Synth. Catal.*, 2003, 345, 103–151.



- 3 M. J. Gilkey and B. Xu, Heterogeneous catalytic transfer hydrogenation as an effective pathway in biomass upgrading, *ACS Catal.*, 2016, **6**, 1420–1436.
- 4 F. Meemken and A. Baiker, Recent progress in heterogeneous asymmetric hydrogenation of C=O and C=C bonds on supported noble metal catalysts, *Chem. Rev.*, 2017, **117**, 11522–11569.
- 5 J. Jia, C. Qian, Y. Dong, Y. F. Li, H. Wang, M. Ghoussoub, K. T. Butler, A. Walsh and G. A. Ozin, Heterogeneous catalytic hydrogenation of CO<sub>2</sub> by metal oxides: defect engineering—perfecting imperfection, *Chem. Soc. Rev.*, 2017, **46**, 4631–4644.
- 6 G. G. Wildgoose, C. E. Banks and R. G. Compton, Metal nanoparticles and related materials supported on carbon nanotubes: methods and applications, *Small*, 2006, **2**, 182–193.
- 7 X.-H. Li and M. Antonietti, Metal nanoparticles at mesoporous N-doped carbons and carbon nitrides: functional Mott–Schottky heterojunctions for catalysis, *Chem. Soc. Rev.*, 2013, **42**, 6593–6604.
- 8 Y. Zhai, Z. Zhu and S. Dong, Carbon-based nanostructures for advanced catalysis, *ChemCatChem*, 2015, **7**, 2806–2815.
- 9 X. Cui, A.-E. Surkus, K. Junge, C. Topf, J. Radnik, C. Kreyenschulte and M. Beller, Highly selective hydrogenation of arenes using nanostructured ruthenium catalysts modified with a carbon–nitrogen matrix, *Nat. Commun.*, 2016, **7**, 11326pp.
- 10 S. Navalon, A. Dhakshinamoorthy, M. Alvaro and H. Garcia, Metal nanoparticles supported on two-dimensional graphenes as heterogeneous catalysts, *Coord. Chem. Rev.*, 2016, **312**, 99–148.
- 11 E. Perez-Mayoral, V. Calvino-Casilda and E. Soriano, Metal-supported carbon-based materials: opportunities and challenges in the synthesis of valuable products, *Catal. Sci. Technol.*, 2016, **6**, 1265–1291.
- 12 H. Zhang, X. Yan, Y. Huang, M. Zhang, Y. Tang, D. Sun, L. Xu and S. Wei, Cyanogel-derived N-doped C nanosheets immobilizing Pd-P nanoparticles: One-pot synthesis and enhanced hydrogenation catalytic performance, *Appl. Surf. Sci.*, 2017, **396**, 812–820.
- 13 R. T. Shuman, P. L. Ornstein, J. W. Paschal and P. D. Gesellchen, An improved synthesis of homoproline and derivatives, *J. Org. Chem.*, 1990, **55**, 738–741.
- 14 A. R. Katritzky, S. Rachwal and B. Rachwal, Recent progress in the synthesis of 1,2,3,4-tetrahydroquinolines, *Tetrahedron*, 1996, **52**, 15031–15070.
- 15 V. Sridharan, P. A. Suryavanshi and J. C. Menéndez, Advances in the chemistry of tetrahydroquinolines, *Chem. Rev.*, 2011, **111**, 7157–7259.
- 16 J. D. Keay, in *Comprehensive Organic Synthesis*, ed. B. M. Trost and I. Fleming, Pergamon, Oxford, 1991, vol. 8, pp. 579–601.
- 17 D. Ren, L. He, L. Yu, R.-S. Ding, Y.-M. Liu, Y. Cao, H.-Y. He and K.-N. Fan, An unusual chemoselective hydrogenation of quinoline compounds using supported gold catalysts, *J. Am. Chem. Soc.*, 2012, **134**, 17592–17598.
- 18 I. S. Park, M. S. Kwon, K. Y. Kang, J. S. Lee and J. Park, Rhodium and iridium nanoparticles entrapped in aluminum oxyhydroxide nanofibers: catalysts for hydrogenations of arenes and ketones at room temperature with hydrogen balloon, *Adv. Synth. Catal.*, 2007, **349**, 2039–2047.
- 19 H. Mao, X. Liao and B. Shi, Amphiphilic tannin-stabilized Rh nanoparticles: A highly active and reusable catalyst in biphasic aqueous-organic system, *Catal. Commun.*, 2011, **16**, 210–214.
- 20 G.-Y. Fan and J. Wu, Mild hydrogenation of quinoline to decahydroquinoline over rhodium nanoparticles entrapped in aluminum oxy-hydroxide, *Catal. Commun.*, 2013, **31**, 81–85.
- 21 H.-Y. Jiang and X.-X. Zheng, Phosphine-functionalized ionic liquid-stabilized rhodium nanoparticles for selective hydrogenation of aromatic compounds, *Appl. Catal., A*, 2015, **499**, 118–123.
- 22 M. Niu, Y. Wang, P. Chen, D. Du, J. Jiang and Z. Jin, Highly efficient and recyclable rhodium nanoparticle catalysts for hydrogenation of quinoline and its derivatives, *Catal. Sci. Technol.*, 2015, **5**, 4746–4749.
- 23 A. Karakulina, A. Gopakumar, İ. Akçok, B. L. Roullet, T. LaGrange, S. A. Katsyuba, S. Das and P. J. Dyson, A rhodium nanoparticle–Lewis acidic ionic liquid catalyst for the chemoselective reduction of heteroarenes, *Angew. Chem.*, 2016, **128**, 300–304.
- 24 F. Martinez-Espinar, P. Blondeau, P. Nolis, B. Chaudret, C. Claver, S. Castillón and C. Godard, NHC-stabilised Rh nanoparticles: Surface study and application in the catalytic hydrogenation of aromatic substrates, *J. Catal.*, 2017, **354**, 113–127.
- 25 A. Karakulina, A. Gopakumar, Z. Fei and P. J. Dyson, Chemoselective reduction of heteroarenes with a reduced graphene oxide supported rhodium nanoparticle catalyst, *Catal. Sci. Technol.*, 2018, **8**, 5091–5097.
- 26 L. Zhang, X. Wang, Y. Xue, X. Zeng, H. Chen, R. Li and S. Wang, Cooperation between the surface hydroxyl groups of Ru–SiO<sub>2</sub>@ mSiO<sub>2</sub> and water for good catalytic performance for hydrogenation of quinoline, *Catal. Sci. Technol.*, 2014, **4**, 1939–1948.
- 27 H. Konnerth and M. H. G. Pechtl, Selective hydrogenation of N-heterocyclic compounds using Ru nanocatalysts in ionic liquids, *Green Chem.*, 2017, **19**, 2762–2767.
- 28 M. M. Dell'Anna, V. F. Capodiferro, M. Mali, D. Manno, P. Cotugno, A. Monopoli and P. Mastrorilli, Highly selective hydrogenation of quinolines promoted by recyclable polymer supported palladium nanoparticles under mild conditions in aqueous medium, *Appl. Catal., A*, 2014, **481**, 89–95.
- 29 L. Bai, X. Wang, Q. Chen, Y. Ye, H. Zheng, J. Guo, Y. Yin and C. Gao, Explaining the size dependence in platinum-nanoparticle-catalyzed hydrogenation reactions, *Angew. Chem., Int. Ed.*, 2016, **55**, 15656–15661.
- 30 F. Leng, I. C. Gerber, P. Lecante, W. Bacsá, J. Miller, J. R. Gallagher, S. Moldovan, M. Girleanu, M. R. Axet and P. Serp, Synthesis and structure of ruthenium-fullerides, *RSC Adv.*, 2016, **6**, 69135–69148.

- 31 F. Leng, I. C. Gerber, P. Lecante, S. Moldovan, M. Girleanu, M. R. Axet and P. Serp, Controlled and chemoselective hydrogenation of nitrobenzene over Ru@C<sub>60</sub> catalysts, *ACS Catal.*, 2016, **6**, 6018–6024.
- 32 M. R. Axet, S. Conejero and I. C. Gerber, Ligand effects on the selective hydrogenation of nitrobenzene to cyclohexylamine using ruthenium nanoparticles as catalyst, *ACS Appl. Nano Mater.*, 2018, **1**, 5885–5894.
- 33 C. Amiens, D. Ciuculescu-Pradines and K. Philippot, Controlled metal nanostructures: Fertile ground for coordination chemists, *Coord. Chem. Rev.*, 2016, **308**, 409–432.
- 34 B. Coq, J. M. Planeix and V. Brotons, Fullerene-based materials as new support media in heterogeneous catalysis by metals, *Appl. Catal., A*, 1998, **173**, 175–183.
- 35 H. Veisi, R. Masti, D. Kordestani, M. Safaei and O. Sahin, Functionalization of fullerene (C<sub>60</sub>) with metformine to immobilized palladium as a novel heterogeneous and reusable nanocatalyst in the Suzuki–Miyaura coupling reaction at room temperature, *J. Mol. Catal. A: Chem.*, 2014, **385**, 61–67.
- 36 H. Keypour, M. Noroozi and A. Rashidi, Schiff base complex method for the preparation of fullerene-based Ni nanocatalyst used in the hydrogenation of benzene in gasoline, *Synth. React. Inorg. Met.-Org. Chem.*, 2015, **45**, 1701–1709.
- 37 T. Braun, M. Wohlers, T. Belz and R. Schlögl, Fullerene-based ruthenium catalysts: a novel approach for anchoring metal to carbonaceous supports. II. Hydrogenation activity, *Catal. Lett.*, 1997, **43**, 175–180.
- 38 M. Lashdaf, A. Hase, E. Kauppinen and A. O. I. Krause, Fullerene-based ruthenium catalysts in cinnamaldehyde hydrogenation, *Catal. Lett.*, 1998, **52**, 199–204.
- 39 M. R. Axet, O. Dechy-Cabaret, J. Durand, M. Gouygou and P. Serp, Coordination chemistry on carbon surfaces, *Coord. Chem. Rev.*, 2016, **308**, 236–345.
- 40 C. Mabille, F. Leal-Calderon, J. Bibette and V. Schmitt, Monodisperse fragmentation in emulsions: mechanisms and kinetics, *Europhys. Lett.*, 2003, **61**, 708–714.
- 41 J. A. Osborn and R. R. Schrock, Coordinatively unsaturated cationic complexes of rhodium(I), iridium(I), palladium(II), and platinum(II). Generation, synthetic utility, and some catalytic studies, *J. Am. Chem. Soc.*, 1971, **93**, 3089–3091.
- 42 M. Green and T. A. Kuc, Cationic transition-metal complexes. II. Reaction of arenes and olefins with bis(1,5-cyclooctadiene or norbornadiene)rhodium tetrafluoroborate, *J. Chem. Soc., Dalton Trans.*, 1972, 832–839.
- 43 R. Uson, L. A. Oro, C. Foces-Foces, F. H. Cano, S. Garcia-Blanco and M. Valderrama, Arene-rhodium(I) complexes with trimethyltetrafluorobenzobarrelene. Crystal structure of [(Me<sub>3</sub>TFB)Rh(p-Me<sub>2</sub>C<sub>6</sub>H<sub>4</sub>)]ClO<sub>4</sub>, *J. Organomet. Chem.*, 1982, **229**, 293–304.
- 44 Y. Abe, K. Kato, M. Kawamura and K. Sasaki, Rhodium and rhodium oxide thin films characterized by XPS, *Surf. Sci. Spectra*, 2001, **8**, 117–125.
- 45 K.-D. Tsuei, J.-Y. Yuh, C.-T. Tzeng, R.-Y. Chu, S.-C. Chung and K.-L. Tsang, Photoemission and photoabsorption study of C<sub>60</sub> adsorption on Cu(111) surfaces, *Phys. Rev. B: Condens. Matter*, 1997, **56**, 15412–15420.
- 46 M. S. Dresselhaus, G. Dresselhaus and P. C. Eklund, Raman scattering in fullerenes, *J. Raman Spectrosc.*, 1996, **27**, 351–371.
- 47 X. H. Chen, X. J. Zhou and S. Roth, Raman scattering in calcium-doped C<sub>60</sub>, *Phys. Rev. B: Condens. Matter*, 1996, **54**, 3971–3975.
- 48 R. A. Jishi and M. S. Dresselhaus, Mode softening and mode stiffening in C<sub>60</sub> doped with alkali metals, *Phys. Rev. B: Condens. Matter*, 1992, **45**, 6914–6918.
- 49 S. Sakai, H. Naramoto, P. V. Avramov, T. Yaita, V. Lavrentiev, K. Narumi, Y. Baba and Y. Maeda, Comparative study of structures and electrical properties in cobalt-fullerene mixtures by systematic change of cobalt content, *Thin Solid Films*, 2007, **515**, 7758–7764.
- 50 L. Becker, T. P. Evans and J. L. Bada, Synthesis of [hydrogenated fullerene] C<sub>60</sub>H<sub>2</sub> by rhodium-catalyzed hydrogenation of C<sub>60</sub>, *J. Org. Chem.*, 1993, **58**, 7630–7631.
- 51 C. Chaudhari, H. Imatome, Y. Nishida, K. Sato and K. Nagaoka, Recyclable Rh-PVP nanoparticles catalyzed hydrogenation of benzoic acid derivatives and quinolines under solvent-free conditions, *Catal. Commun.*, 2019, **126**, 55–60.
- 52 M. Mateen, K. Shah, Z. Chen, C. Chen and Y. Li, Selective hydrogenation of N-heterocyclic compounds over rhodium-copper bimetallic nanocrystals under ambient conditions, *Nano Res.*, 2019, **12**, 1631–1634.
- 53 Z. Wei, Y. Chen, J. Wang, D. Su, M. Tang, S. Mao and Y. Wang, Cobalt encapsulated in N-doped graphene layers: an efficient and stable catalyst for hydrogenation of quinoline compounds, *ACS Catal.*, 2016, **6**, 5816–5822.
- 54 Y.-P. Sun, H.-Y. Fu, D.-I. Zhang, R.-X. Li, H. Chen and X.-J. Li, Complete hydrogenation of quinoline over hydroxyapatite supported ruthenium catalyst, *Catal. Commun.*, 2010, **12**, 188–192.
- 55 Y. Gong, P. Zhang, X. Xu, Y. Li, H. Li and Y. Wang, A novel catalyst Pd@ ompg-C<sub>3</sub>N<sub>4</sub> for highly chemoselective hydrogenation of quinoline under mild conditions, *J. Catal.*, 2013, **297**, 272–280.
- 56 R. A. Sánchez-Delgado and N. Machalaba, Hydrogenation of quinoline by ruthenium nanoparticles immobilized on poly(4-vinylpyridine), *Catal. Commun.*, 2007, **8**, 2115–2118.
- 57 B. Sun, F.-A. Khan, A. Vallat and G. Süß-Fink, NanoRu@ hectorite: a heterogeneous catalyst with switchable selectivity for the hydrogenation of quinoline, *Appl. Catal., A*, 2013, **467**, 310–314.
- 58 H. Mao, J. Ma, Y. Liao, S. Zhao and X. Liao, Using plant tannin as natural amphiphilic stabilizer to construct an aqueous-organic biphasic system for highly active and selective hydrogenation of quinoline, *Catal. Sci. Technol.*, 2013, **3**, 1612–1617.
- 59 L. M. Martinez-Prieto and B. Chaudret, Organometallic ruthenium nanoparticles: synthesis, surface chemistry, and insights into ligand coordination, *Acc. Chem. Res.*, 2018, **51**, 376–384.

- 60 J. H. Scofield, Hartree-Slater subshell photoionization cross-sections at 1254 and 1487 eV, *J. Electron Spectrosc. Relat. Phenom.*, 1976, 8, 129–137.
- 61 G. Kresse and J. Furthmüller, Efficiency of ab-initio total energy calculations for metals and semiconductors using a plane-wave basis set, *Comput. Mater. Sci.*, 1996, 6, 15–50.
- 62 G. Kresse and J. Hafner, Ab initio molecular dynamics for liquid metals, *Phys. Rev. B*, 1993, 47, 558–561.
- 63 G. Kresse and J. Furthmüller, Efficient iterative schemes for *ab initio* total-energy calculations using a plane-wave basis set, *Phys. Rev. B*, 1996, 54, 11169–11186.
- 64 G. Kresse and J. Hafner, Ab initio molecular-dynamics simulation of the liquid-metal-amorphous-semiconductor transition in germanium, *Phys. Rev. B*, 1994, 49, 14251–14269.
- 65 P. E. Blöchl, Projector augmented-wave method, *Phys. Rev. B*, 1994, 50, 17953–17979.
- 66 G. Kresse and D. Joubert, From ultrasoft pseudopotentials to the projector augmented-wave method, *Phys. Rev. B*, 1999, 59, 1758–1775.
- 67 J. P. Perdew, K. Burke and M. Ernzerhof, Generalized gradient approximation made simple, *Phys. Rev. Lett.*, 1996, 77, 3865–3868.
- 68 K. Momma and F. Izumi, VESTA 3 for three-dimensional visualization of crystal, volumetric and morphology data, *J. Appl. Crystallogr.*, 2011, 44, 1272–1276.
- 69 W. Tang, E. Sanville and G. Henkelman, A grid-based Bader analysis algorithm without lattice bias, *J. Phys.: Condens. Matter*, 2009, 21, 084204/1–084204/7.
- 70 I. del Rosal, L. Truflandier, R. Poteau and I. C. Gerber, A density functional theory study of spectroscopic and thermodynamic properties of surfacic hydrides on Ru (0001) model surface: the influence of the coordination modes and the coverage, *J. Phys. Chem. C*, 2011, 115, 2169–2178.